Results in Applied Mathematics 18 (2023) 100374

Contents lists available at ScienceDirect

Results in Applied Mathematics

journal homepage: www.elsevier.com/locate/results-in-applied-mathematics

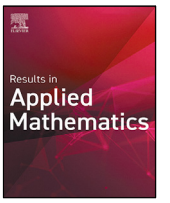

A non-hydrostatic model for wave evolution on a submerged trapezoidal breakwater

Ikha Magdalena [a,b,*], Hany Q. Rif'atin [b], M. Syahril Badri Kusuma [b,c], Dominic E. Reeve [d]

[a] Faculty of Mathematics and Natural Sciences, Bandung Institute of Technology, Bandung, Indonesia
[b] Center for Coastal and Marine Development, Bandung Institute of Technology, Bandung, Indonesia
[c] Faculty of Civil and Environmental Engineering, Bandung Institute of Technology, Bandung, Indonesia
[d] College of Engineering, Swansea University, Bay Campus, Swansea SA2 8PP, UK

ARTICLE INFO

Article history:
Received 20 January 2023
Received in revised form 2 April 2023
Accepted 24 April 2023
Available online 4 May 2023

Keywords:
Wave propagation
Non-hydrostatic model
Predictor–corrector procedure
Composite-slope trapezoidal breakwater

ABSTRACT

A depth-averaged non-hydrostatic model is formulated to investigate wave evolution on a water channel with a submerged trapezoidal breakwater. This model is an extension of nonlinear shallow water equations that includes hydrodynamic pressure and vertical velocity. In the momentum equation, a diffusion term is also considered to represent the turbulence effects in the system. The equations are solved numerically using a combination of a staggered finite volume method and predictor–corrector procedure. Comparisons are made against three independent laboratory experiments of wave propagation over submerged breakwaters. The level of agreement is higher than with Boussinesq-type and RANS models. The numerical scheme is also used to study the effect of the height, length, and diffusion coefficient of the breakwater on wave propagation. We have found that those characteristics affect the wave similarly by smoothing the wave shape and significantly reducing the transmitted wave amplitude.

1. Introduction

Low-crested structures (breakwaters) are increasingly used by coastal engineers and planners because of their function as a sea defence. Low-crested breakwaters are essentially constructed with the crown elevation near the still water level. Such breakwater systems may be submerged or emergent, but here we concentrate only on the submerged type. This sort of structure is typically located close and parallel to the shoreline, either to protect sections of shoreline from erosion or to provide shelter for boats. The main function of these structures is to keep the waves calm along the coast. Normally, waves approaching the shore over a sloping beach will gradually rise due to the process of shoaling until they become unstable and begin to break [1]. Submerged breakwaters act as partial reflectors and dissipators, as well as promote wave breaking under certain circumstances [2]. Submerged breakwaters tend to change the waveform of the incident waves, so it is crucial to study the evolution of waves before and after their interaction with the breakwater.

Early studies developed analytical approaches such as Lamb's investigation of the propagation of waves over an infinite step [3]. This was later extended by Jeffreys [4] and Mei [5], who studied the case of breakwaters with rectangular cross-sections. The shape of the breakwater was further generalized to a trapezoidal shape by Lin & Liu [6]. However, analytical approaches are largely restricted to the solution of linear and hydrostatic problems, which is an idealization

* Corresponding author at: Faculty of Mathematics and Natural Sciences, Bandung Institute of Technology, Bandung, Indonesia.
E-mail address: ikha.magdalena@itb.ac.id (I. Magdalena).

https://doi.org/10.1016/j.rinam.2023.100374

rarely found in real life. As a result, researchers such as Rey et al. [7] and Stamos & Hajj [8] performed scaled laboratory experiments to study wave propagation over rectangular breakwaters. The impact of variations in geometrical cross-section was investigated by Beji & Bettjes [9] and Ohyama et al. [10], who studied trapezoidal cross-sections, whereas Garcia et al. [11] and Kramer et al. [12] examined the case of composite-sloped trapezoidal breakwaters. While affording an excellent facsimile of reality, scale model experiments can suffer from scale-related distortion effects due to surface tension [13,14], are relatively inflexible in terms of the effort required to alter the geometry, and are costly to perform.

The growing availability of computers led to the emergence of computational methods to study wave propagation around obstacles [15–18], and waves interaction with porous and flexible structures [19–26]. Using similar models and methods, which are Shallow Water Equations and Finite Volume Method on a Staggered Grid, respectively, Magdalena et al. [15], and Magdalena et al. [18] studied different wave occurrences with different shapes of breakwater as well. Magdalena et al. [15] investigated wave propagation over n-block rectangular breakwater and were able to determine an optimum length of the structure for one block case. Meanwhile, Magdalena et al. [18] assessed dam break phenomena if there is a trapezoidal, triangular, or coupled-trapezoidal obstacles located in several different point in the observation domain. A trapezoidal submerged breakwater was also examined by Repousis et al. [16] using Boussinesq coupled with Darcy–Forchheimer equation and applying the parameterization of crucial coefficients of the breaking module in the model. Investigating different wave occurrence, which is waves propagation caused by an explosion, Soukup et al. [17] applied Finite Element method on the Navier–Stokes equations and studied the phenomena if a bar or trench is involved. In studying wave evolution when porous breakwaters were considered, Wiryanto [19], Magdalena et al. [21], Firdaus et al. [22], and Magdalena and Michael [23] used models related to Shallow Water Equations with different methods, bathymetry, and waves characteristics. However, all of these studies resulted in the same conclusion in which porous breakwater reduces wave transmitted amplitude effectively. Extending the studies by considering a flexible porous breakwater in the model based on the Green's function, Williams and Wang [20] were also able to determine the optimal structural parameters such that the flexible breakwater can be an effective wave barrier. Wave scattering and wave trapping were examined by Tabssum et al. [24], Sharma et al. [25], and Singh and Kaligatla [26] with different models, methods, and structures. [24] assess the phenomena for bottom-standing and surface-piercing partial porous breakwater using Eigenfunction expansion and Mild-slope equation on solving the Potential Flow Theory. Meanwhile, [25] use the same methods to solve Sollitt and Cross' model for trapezoidal, circular, and wadge shapes porous breakwater. Differently, [26] apply Eigenfunction and Galerkin-Eigenfunction expansion in solving Water wave theory coupled with Darcy Law for wave scattering and Green's function for structure deflection. Computational studies have focused mainly on either nonlinear, nonlinear non-dispersive long waves [27] or dispersive Boussinesq waves [28]. Shallow water equations provide an excellent approximation for wave propagation when the wave length (L) is greater than twenty times the water depth (h) [29, part 1, ch. 2, pp, 38-45]. Boussinesq equations retain some dispersive and nonlinear aspects of wave propagation, and accurately resolve wave propagation in deeper water, up to $h/L \approx 0.5$ [29]. Both models simplify the flow dynamics by integrating over water depth, while retaining an element of the effect of vertical structure of the flow under waves. Such models have become known as 2DH (two-dimensional in the horizontal) models or 1DH in the case of an on–offshore transect. Both models are popular in engineering applications as they often provide a good balance between accuracy and computational cost. The derivation of nonlinear shallow water equations may be found in [30,31], while a thorough derivation of Boussinesq equations for water wave propagation may be found in [32]. Reviews of several variants of Boussinesq-type equations, computational approximations, and comparative performance may be found in [33,34].

Both Boussinesq equations and nonlinear shallow water equations (NSWE) have limitations in the nearshore region. Neither can naturally simulate wave breaking, and Boussinesq models become extremely demanding to solve computationally due to the high-order derivatives in the equations. While the wave breaking problem has become tractable through the solution of Reynolds Averaged Navier–Stokes equations with turbulence sub-models [35,36], such techniques remain incredibly expensive. The need for accurate yet computationally reasonable wave propagation models for engineering applications remains. In this study, we formulate a numerical model based on the NSWE that can capture wave dispersion and is efficient to solve. It is tested in the case of a submerged trapezoidal breakwater. The starting point is a depth-averaged non-hydrostatic formulation of the NSWE. The non-hydrostatic component consists of the hydrodynamic pressure and vertical velocity. We also include a diffusion term as a simple representation of the turbulent dissipation [37]. The equations are solved using a Staggered Finite Volume Method combined with the predictor–corrector procedure. Then, the numerical model is validated for several experimental measurements in order to verify the hydrostatic and hydrodynamic aspects of the model.

The paper is divided into five sections, including this introduction. The second section provides an explanation of the non-hydrostatic model. The numerical solution of the equations is described in Section 3. The model results are presented in the fourth section, compared to the experimental data as well as Boussinesq and RANS model results for three different cases. The results of a computational sensitivity study, investigating the dependence of wave transmission on the breakwater crest height, and length are also discussed in this section. The paper closes with a brief set of conclusions.

2. Non-hydrostatic model

In this section, a one-layer non-hydrostatic model is developed to analyse the propagation of waves over a submerged obstacle. The model is a modification of the NSWE that includes hydrodynamic pressure and vertical velocity, thereby retaining wave dispersion.

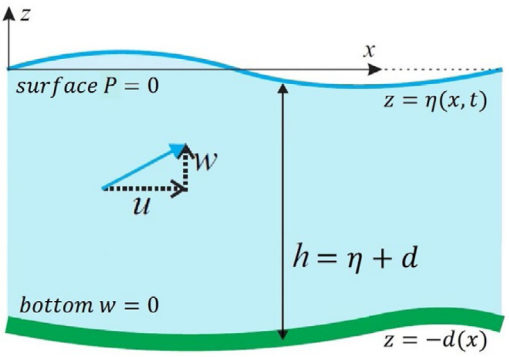

Fig. 1. Illustration of a one-layer non-hydrostatic model.

Fig. 1 illustrates the main elements of the model. Mathematically, the model can be written as two equations, mass conservation and momentum balance, which read as

$$\eta_t + (hu)_x = 0, \tag{1}$$

$$u_t + uu_x + g\eta_x - \kappa u_{xx} = -\frac{1}{h}\int_{-d}^{\eta} \frac{\partial P}{\partial x} dz. \tag{2}$$

where $\eta(x, t)$ denotes the surface elevation of the water and $u(x, t)$ is the depth-integrated horizontal velocity. The total water depth is $h = \eta + d$ where d is the water depth measured from the undisturbed water position, g is the Earth's gravitational acceleration, and $P(x, z)$ is the hydrodynamic pressure of the water. At the water surface, $(z = \eta)$, the hydrodynamic pressure is taken to be zero and a linearized vertical momentum equation is assumed to hold

$$w_t = -P_z, \tag{3}$$

where w is the vertical velocity. The seabed is assumed rigid and impermeable, so that $w = 0$ on $z = -d$. Energy losses due to turbulent diffusion are modelled by a diffusion term that is included in the momentum conservation equation as κu_{xx} where κ is the diffusion coefficient [38,39].

3. Numerical scheme formulation

In this section, we present the numerical scheme developed to solve the non-hydrostatic model equations. The scheme consists of two steps: a predictor step and a corrector step. In the predictor step, the numerical scheme for the hydrostatic part of the equations is formed using the finite volume on a staggered grid. Staggered grid was chosen since not only it is free from damping error, but it will also avoid the Riemann problem that is involved if we apply finite volume method on a collocated grid. Further, in the corrector step, the hydrodynamic pressure is computed and used to calculate an updated value of the velocity that meets an incompressibility criterion. The values of η and u obtained in the first step are the predictors, which will be corrected in the second step by including hydrodynamic pressure and vertical velocity in the equations.

3.1. Predictor step

During this step, we solve Eqs. (1) and (2) without hydrodynamic pressure P. Thus,

$$\eta_t + (hu)_x = 0, \tag{4}$$

$$u_t + uu_x + g\eta_x - \kappa u_{xx} = 0. \tag{5}$$

Considering the observation domain of $[0, L]$, the staggered grid is defined by $x_{\frac{1}{2}} = 0, x_1, x_{\frac{3}{2}}, x_2, \ldots, x_{Nx}, x_{Nx+\frac{1}{2}} = L$. As illustrated in Fig. 2, the values of surface elevations η are computed at every full-grid point $x_i = i\Delta x$, with $i = 1, 2, \ldots, Nx$ using mass conservation Eq. (4). The horizontal velocities, u, are computed at half-grid points $x_{i+\frac{1}{2}} = (i + \frac{1}{2})\Delta x$, in which $i = 0, 1, 2, \ldots, Nx$ using the momentum balance equation, Eq. (5). Hence, in this case, we will only need to handle one variable (u) at the boundaries, which are located at the half-points.

Using finite volume method on the staggered grid, we approximate Eqs. (4) and (5), respectively, with the following schemes:

$$\frac{\eta_i^{n+1} - \eta_i^n}{\Delta t} + \frac{{}^*hu|_{i+1/2}^n - {}^*hu|_{i-1/2}^n}{\Delta x} = 0, \tag{6}$$

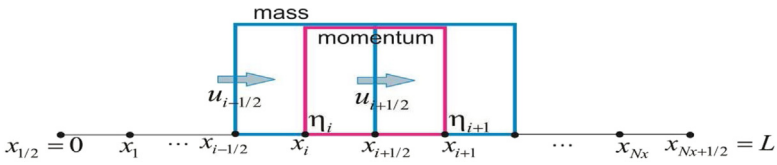

Fig. 2. The configuration of calculated variables η and u on a staggered grid definition.

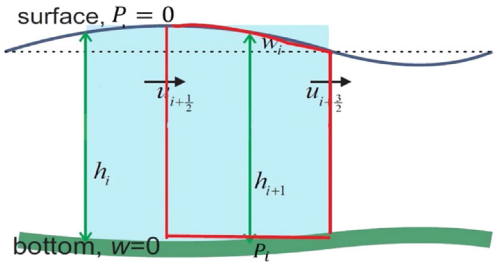

Fig. 3. Illustration of finite volume method on a staggered grid in the non-hydrostatic model.

$$\frac{u_{i+1/2}^{n+1}-u_{i+1/2}^{n}}{\Delta t}+g\frac{\eta_{i+1}^{n+1}-\eta_{i}^{n+1}}{\Delta x}+(uu_x)_{i+\frac{1}{2}}^{n}-\kappa\frac{u_{i+3/2}^{n}-2u_{i+1/2}^{n}+u_{i-1/2}^{n}}{\Delta x^2}=0. \tag{7}$$

Since the water depth $h=\eta+d$ is also known on the full-grid points, its value required at half-grid points in Eq. (6) is unknown and denoted by ${}^*h$. Thus, the first order upwind method is used to approximate the unknown values ${}^*h$, such that

$${}^*h_{i+1/2}=\begin{cases}h_i, & if \quad u_{i+1/2}\geq 0,\\ h_{i+1}, & if \quad u_{i+1/2}<0.\end{cases} \tag{8}$$

The advection term, uu_x, is approximated by first introducing the flux, $q=hu$, and rewriting the term as

$$uu_x=\frac{1}{h}\left(\frac{\partial(qu)}{\partial x}-u\frac{\partial q}{\partial x}\right). \tag{9}$$

Then, the discretization for the advection term (9) is

$$(uu_x)_{i+1/2}=\frac{1}{\overline{h}_{i+1/2}}\left(\frac{\overline{q}_{i+1}{}^*u_{i+1}-\overline{q}_i{}^*u_i}{\Delta x}-u_{i+1/2}\frac{\overline{q}_{i+1}-\overline{q}_i}{\Delta x}\right), \tag{10}$$

where the value of the barred variables are basically the averages of the variable calculated from the two closest whole or half-points. Thus,

$$\overline{h}_{i+1/2}=\frac{(h_i+h_{i+1})}{2},\ \overline{q}_i=\frac{(q_{i+1/2}+q_{i-1/2})}{2},\ q_{i+1/2}={}^*h_{i+1/2}u_{i+1/2}.$$

In a manner similar to the method used for approximating ${}^*h$, where values of u are required at whole grid-points, we use the first order upwind method to estimate the required quantities such that

$${}^*u_i=\begin{cases}u_{i-1/2}, & if \quad \overline{q}_i\geq 0,\\ u_{i+1/2}, & if \quad \overline{q}_i<0.\end{cases} \tag{11}$$

In conclusion, the numerical schemes used to approximate the mass conservation Eq. (4) are (6) and (8), while the approximation schemes for the momentum conservation equation are (5), (7), (10) and (11). The value of u produced by this scheme is the predictor which will be corrected in the next part. The illustration of this scheme can be found in Fig. 3.

3.2. Corrector step

For the corrector step, the effect of the hydrodynamic pressure term P in the momentum equation is determined. First, from Leibniz's rule, the right-hand side of Eq. (2) may be rewritten as

$$\int_{-d}^{\eta}\frac{\partial P}{\partial x}dz=\frac{\partial}{\partial x}\int_{-d}^{\eta}Pdz-P|_{z=-d}\frac{\partial d}{\partial x}-P|_{z=\eta}\frac{\partial \eta}{\partial x}. \tag{12}$$

Notations $|_{z=\eta}$ and $|_{z=-d}$ indicate that the quantities are evaluated at the surface and seabed, respectively. The integral term on the right-hand side of Eq. (12) is approximated with a simple trapezoidal expression:

$$\int_{-d}^{\eta} P dz \simeq \frac{1}{2} h(P|_{z=\eta} + P|_{z=-d}).$$

As $P|_{z=\eta} = 0$, Eq. (12) can be simplified to

$$\int_{-d}^{\eta} \frac{\partial P}{\partial x} dz = \frac{1}{2} h \frac{\partial P|_{z=-d}}{\partial x} + \frac{1}{2} P|_{z=-d} \frac{\partial h}{\partial x} - P|_{z=-d} \frac{\partial d}{\partial x} = \frac{1}{2} h \frac{\partial P|_{z=-d}}{\partial x} + \frac{1}{2} P|_{z=-d} \frac{\partial(\eta - d)}{\partial x}. \tag{13}$$

Consequently, the approximated momentum equation reads as

$$u_t + u u_x + g\eta_x - \kappa u_{xx} = -\frac{1}{2} \frac{\partial P|_{z=-d}}{\partial x} - \frac{1}{2h} P|_{z=-d} \frac{\partial(\eta - d)}{\partial x}. \tag{14}$$

We may also use Eq. (3) to find the vertical velocity at the surface from the pressure by applying the Keller-box scheme to yield

$$\frac{w^{n+1}|_{z=\eta} - w^n|_{z=\eta} + w^{n+1}|_{z=-d} - w^n|_{z=-d}}{2\Delta t} = -\frac{P^{n+1}|_{z=\eta} - P^{n+1}|_{z=-d}}{h^{n+1}}. \tag{15}$$

Now, due to the impermeability of the seabed, the vertical velocity is zero at $z = -d$, so we can write $w|_{z=-d} = 0$. Since the hydrodynamic pressure is zero at the surface ($P|_{z=\eta} = 0$), so Eq. (15) simplifies to

$$\frac{w^{n+1}|_{z=\eta} - w^n|_{z=\eta}}{2\Delta t} = \frac{P^{n+1}|_{z=-d}}{h^{n+1}}, \tag{16}$$

and hence

$$w_i^{n+1}|_{z=\eta} = w_i^n|_{z=\eta} + 2\Delta t \frac{P_i^{n+1}|_{z=-d}}{h_i^{n+1}}. \tag{17}$$

So, once the pressure is determined at the new time step, the corresponding value of vertical velocity may be found directly. The calculation of the pressure follows from imposing the incompressibility criterion, or

$$u_x + w_z = 0.$$

Replacing the derivative of w with a simple finite difference equivalent based on values at the surface and seabed, and recalling that $w|_{z=-d} = 0$, we find

$$u_x + \frac{w|_{z=\eta}}{h} = 0, \tag{18}$$

and its finite difference equivalent

$$w_i^n + h_i^n \frac{u_{i+1/2}^n - u_{i-1/2}^n}{\Delta x} = 0. \tag{19}$$

Now, the correction for the velocity u is given by:

$$u_{i+1/2}^{n+1} = {u_{i+1/2}}^* - \Delta t \frac{P_{i+1}^{n+1}|_{z=-d} - P_i^{n+1}|_{z=-d}}{2\Delta x}, \tag{20}$$

where u^* is the value of u calculated after completing the predictor step. Substituting Eqs. (17) and (20) into Eq. (19) results in a tridiagonal system of equations for P_i which may be solved efficiently using, for example, the Thomas Algorithm [40]. Using hydrodynamic pressure and vertical velocity to correct the velocity produced by the hydrostatic part, this scheme has the ability to handle dispersion and makes a better approximation of the actual wave propagation [41].

To summarize, the computational procedure is as follows:

1. The fluid is taken to be at rest initially with $u = w = \eta = 0$ everywhere and $P|_{z=\eta} = 0$;
2. Wave motion is initiated at the lefthand boundary by specifying a sequence of sinusoidally varying surface elevation;
3. A predictor step is taken using Eqs. (6)–(8), and (10)–(11);
4. The tridiagonal system for P_i is solved using Thomas Algorithm;
5. The corrector step for the horizontal velocity is made using Eq. (20);
6. The vertical velocity is updated from the pressure through Eq. (17).

4. Result and discussion

In this section, we compare the performance of the non-hydrostatic model to three regular wave cases. These are: waves propagating over an asymmetric trapezoidal breakwater with gentle side slopes; waves propagating over a

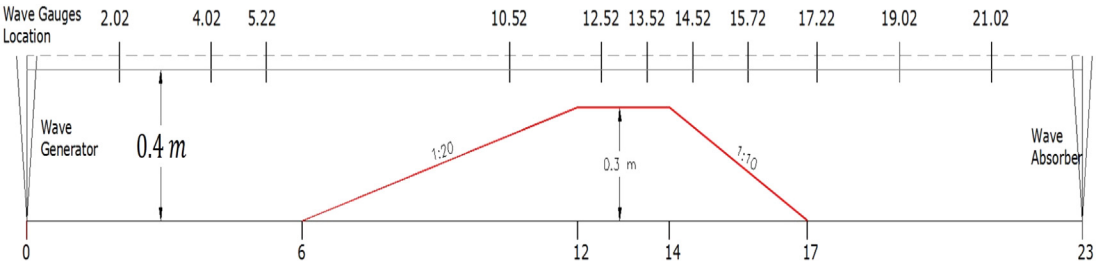

Fig. 4. Measurement points around and on the structure. All units are in m.
Source: Picture is adopted from [9].

Table 1
Incident Wave Characteristics for Delft Experiments Case 1 and 2.

Characteristics	Case 1	Case 2
Wave amplitude (m)	0.01	0.0205
Wave period (s)	2.02	1.01

symmetric trapezoidal breakwater with steep side slopes; and waves propagating over an asymmetric composite sloped breakwater. These three scenarios were chosen because the first two involve typical breakwater shapes that are frequently used in laboratory experiments or in real life; thus, the two cases are appropriate for model validations. The last scenario was chosen because it represents the general shape of a breakwater, allowing the proposed model's capacity to estimate wave evolution over the breakwater to be thoroughly evaluated. For each case, we compare the results from our model with the experimental measurements and published results obtained from the Boussinesq or RANS-VOF models.

4.1. Delft experiment

In one of the earliest experimental studies on the topic, Beji & Battjes [9] undertook a series of wave tank experiments at Delft University to investigate wave propagation over submerged breakwaters. Dingemans [28] subsequently used a Boussinesq-type model to simulate the same cases. The experimental set-up used by Beji & Battjes [9] is shown in Fig. 4. The still water level was 0.4 m above the flat bottom of the tank, and the height of the crest of the breakwater was 0.3 m. The offshore slope is 1/20 while the shoreward slope is 1/10. The initial condition is still water. In performing the simulations, both Boussinesq and Non-hydrostatic model use spatial step of $\Delta x = 0.05$ m and a time step of $\Delta t = 0.01$ s, so that the results obtained from both models can be compared fairly. Additionally, a certain coefficient is needed to be able to perform the Boussinesq model, which is donated by $B = 1/15$ and determined by matching the linear dispersion relation with a polynomial expansion of Stokes first order theory combined with the use of Pade's approximant. Waves were generated by a paddle at the left-hand boundary, approximately 6 m from the toe of the leading slope of the breakwater. Wave gauges were positioned along the wave tank as indicated in Fig. 4. The incident wave characteristics for two cases that are investigated are summarized in Table 1, while the gravity acceleration is set to be $g = 9.81$ m/s^2.

The layout shown in Fig. 4 was replicated in our model with an absorbing boundary at the right-hand end of the domain. Comparisons of the experimental results (red), the Boussinesq model of [28] (black), and our non-hydrostatic model (blue) for Case 1 at eight wave gauges are shown in Fig. 5. Corresponding plots for Case 2 are shown in Fig. 6. For this simulation, the turbulence is omitted from the non-hydrostatic model proposed.

For the longer wave case (Fig. 5), the regular wave profile is distorted slightly on the leading side of the breakwater (x = 10.5 m), is distorted strongly over the crest of the breakwater, and exhibits higher frequency harmonics as it propagates beyond the breakwater. The generation of higher frequency harmonics is an example of the eponymous Benjamin–Feir instability phenomenon [42], in which deviations from a periodic waveform are amplified by nonlinearity, leading to the generation of higher frequency harmonics and the eventual disintegration of the waveform into a sequence of individual pulses or, in some cases, the recovery of a regular waveform. The nonlinear behaviour over the crest and downward slope is captured well by the Boussinesq model of [28], and our model provides closer agreement with the experimental results, particularly beyond the breakwater. This statement is supported by Table 2 which lists the Root Mean Square Error (RMSE) of the Boussinesq model and the proposed model, compared to the experimental data measured for Case 1.

For the shorter waves (Fig. 6), some asymmetry in the waveform is evident as the wave propagates over the breakwater, but the original waveform is almost regained once the wave propagates past the trailing edge of the breakwater. Again, reasonable agreement with observations is achieved by the Boussinesq model, but our model provides closer agreement, especially in the down-slope region of the breakwater (x = 15.7 m, $x = 17.3$ m), where there are major phase errors in the Boussinesq model predictions. This can also be seen from the RMSE shown in Table 3.

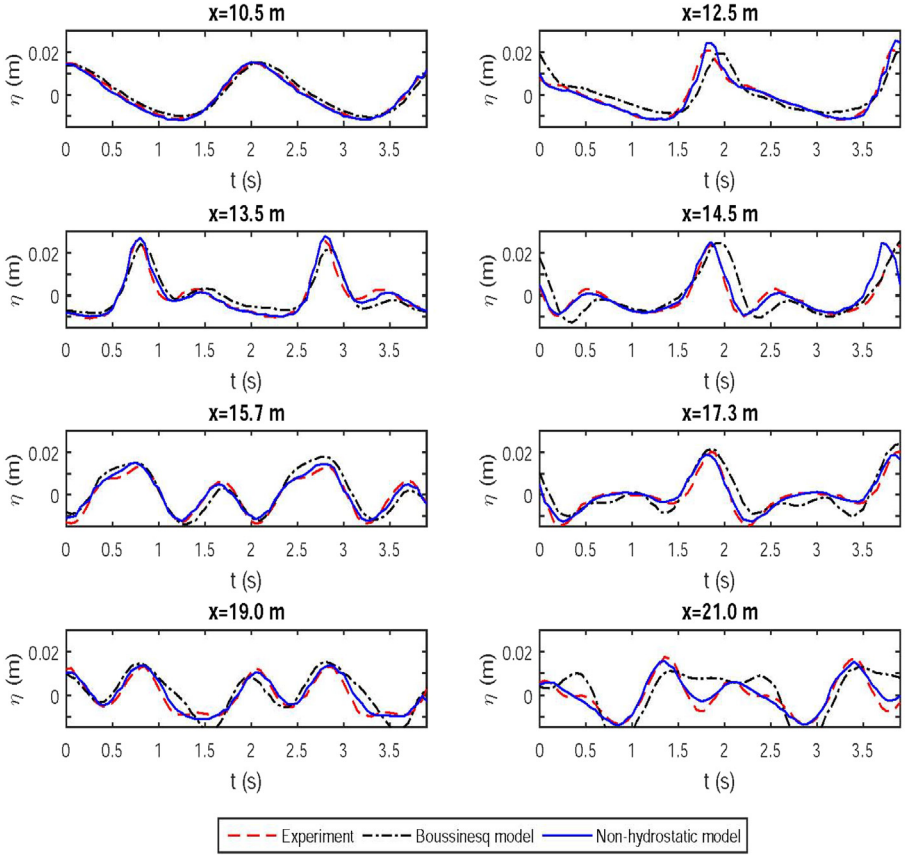

Fig. 5. Comparisons of the free surface elevations for Case 1.

Table 2
The errors of Boussinesq and Non-hydrostatic results compared to the experimental data for Case 1 of Delft Experiment, calculated using Root Mean Square Error (RMSE) method.

x (m)	RMSE (m)	
	Boussinesq-experiment	Non-hydrostatic-experiment
10.5	0.001507974	0.000839131
12.5	0.004802898	0.001909191
13.5	0.003757327	0.002018741
14.5	0.006508216	0.003957506
15.7	0.003794598	0.001841376
17.3	0.004802866	0.001981912
19.0	0.005083362	0.002091426
21.0	0.008276463	0.002330000

In addition, the computational times of both models are listed in Table 4, with the specifications of the computer used to perform the numerical simulations are shown in Table 5. Table 4 only shows the computational time for Case 2, since both cases are basically the same with differences only in few parameters. It is clear from Table 4 that the proposed Non-hydrostatic model conducted a faster simulation compared to the Boussinesq model. One of the reason is because of the higher-order derivatives of the surface elevation variable (in this paper, η) that are involved in Boussinesq model, which are η_{xx} and η_{xxx}. In the numerical computation, these terms are calculated using more grid points compared to the first-order derivative, hence, the model need more time to perform. The same terms were absent in the proposed model, thus, leads to a smaller computational time.

4.2. Ohyama experiment

Ohyama et al. [10] investigated the propagation of waves over a submerged trapezoidal breakwater with much steeper sides than in the Delft Experiment. In this segment, we present comparisons between the results of our non-hydrostatic

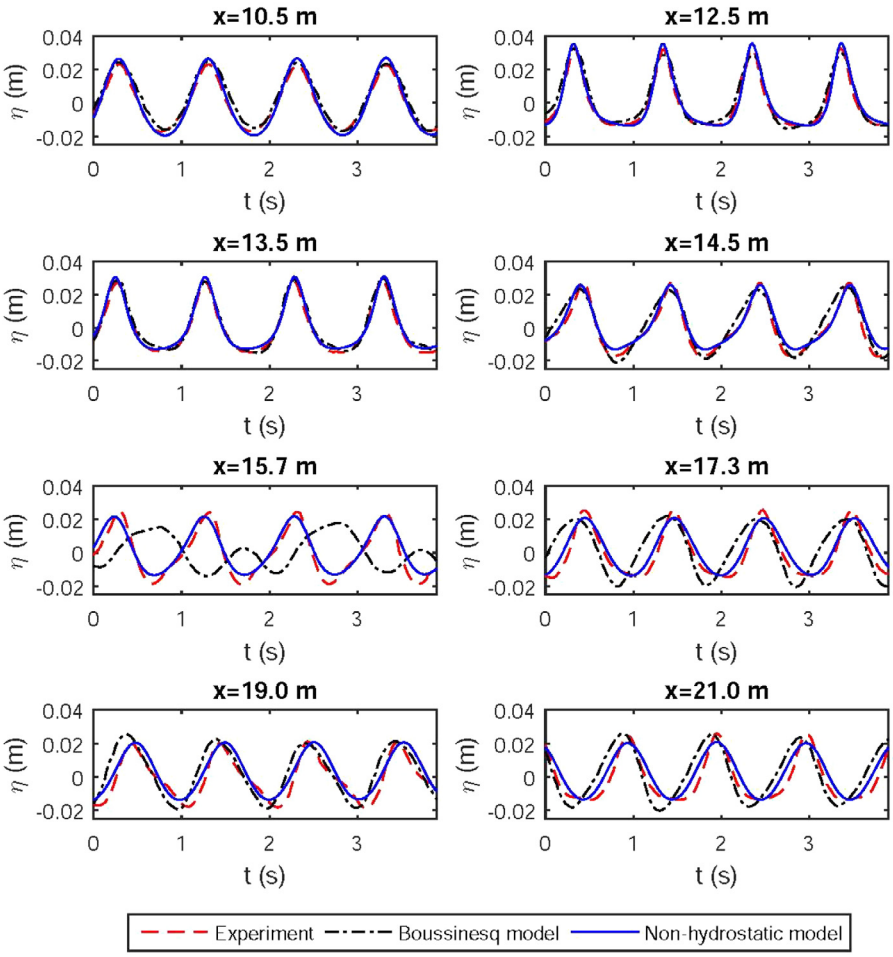

Fig. 6. Comparisons of the free surface elevations for Case 2.

Table 3
The errors of Boussinesq and Non-hydrostatic results compared to the experimental data for Case 2 of Delft Experiment, calculated using Root Mean Square Error (RMSE) method.

x (m)	RMSE (m)	
	Boussinesq-experiment	Nonhydrostatic-experiment
10.5	0.003698308	0.002730289
12.5	0.003437232	0.002563913
13.5	0.002566503	0.004022346
14.5	0.004838718	0.005010833
15.7	0.000442935	0.000031449
17.3	0.011439900	0.004551060
19.0	0.008337077	0.006603409
21.0	0.009604232	0.005202272

Table 4
The computational time of Non-hydrostatic model and Boussinesq model on simulating Case 2 of Delft Experiment.

Model	Time (s)
Non-hydrostatic	0.086543
Boussinesq	0.115173

Table 5
Computer specification and MATLAB version that are used to perform the simulations.

Technical requirement	Specification
Operating System	macOS Ventura Version 13.1
Chip/ CPU/ GPU	Apple M2/ 8 – core/ 8 - core
RAM	8 GB
MATLAB version	R2022b

Table 6
Wave characteristics used for Cases 2, 4, and 6 in the Ohyama experiment.

Characteristics	Case 2	Case 4	Case 6
Wave height (m)	0.2	0.2	0.2
Wave period (s)	1.34	2.01	2.68

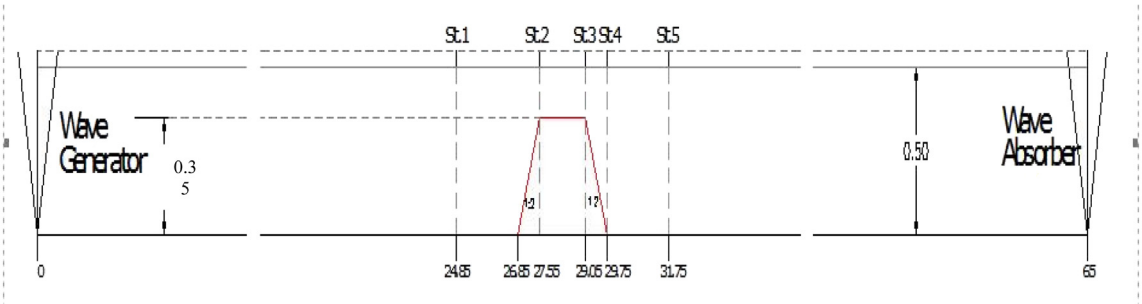

Fig. 7. Sketch of wave flume of the Ohyama Experiment [10]. All units are in m.

model, the Ohyama experiment measurements, and the numerical results given by the Boussinesq model described in [10]. Note that turbulence is excluded from the numerical simulations of this case. An illustration of the set-up and the gauge locations is presented in Fig. 7.

The experiment was conducted in a wave flume 65 m long and 1.0 m wide. The total depth of the flume was 1.6 m. The centre of the breakwater was located at 28.3 m from the wave generator. Waves generated at the lefthand side of Fig. 7 were absorbed at the righthand end of the flume. The measurements of surface elevation were performed at 5 gauges or stations, which are Station 1, 2, 3, 4, and 5, located at $x = 24.85$ m, 27.55 m, 29.05 m, 29.75 m, and 31.85 m, respectively. In total, there are six tests that were carried out using three distinct incoming wave periods (1.34 s, 2.01 s, 2.68 s) and two wave heights (0.1 m, 0.2 m). In all cases, the undisturbed water depth was 0.5 m. However, for the comparisons, we consider measurements taken at Station 3 and Station 5, for 3 cases, as detailed in Table 6.

The layout shown in Fig. 7 was replicated in our model with an absorbing boundary at the right-hand end of the domain. Comparisons of the experimental results (red), the Boussinesq model of [10] (black), and our non-hydrostatic model (blue) for the three cases at Stations 3 and 5 are shown in Fig. 8. The numerical simulations are conducted with a spatial grid spacing of $\Delta x = 0.05$ m, a time step of $\Delta t = 0.01$ s, and a gravitational acceleration of $g = 9.81$ m/s^2. The initial condition is the fluid at rest. These parameters and initial condition are the same for both numerical models. In addition, we use the same coefficient $B = 1/15$ in the Boussinesq model.

As in the Delft Experiment, distortion of the initially regular waveform is evident at Station 3 in Case 2 and 6. In Case 4, some higher-frequency harmonics are clearly evident. At Station 5, beyond the breakwater, the original waveform has disintegrated into multiple harmonics. The Boussinesq model captures the amplitudes well but experiences some difficulties in consistently reproducing wave phase. Our non-hydrostatic model performs better than the Boussinesq model in this case too, since the overall Root Mean Square Error (RMSE) of the Boussinesq model is 0.042 m, while it is 0.037 m for the non-hydrostatic model. Our model performs best on Case 6, which is also the case with the longest wave length. That a shallow water equations model does best in this case is perhaps to be expected. Moreover, the computational times of both models in simulating Case 2 are listed in Table 7. The computer and software specifications are the same as the ones listed in Table 5. It can be seen that the computational time of Non-hydrostatic model is smaller than Boussinesq model, consistent with the results from previous subsection.

4.3. The DELOS project

The third and final test case involves measurements from an experiment from the DELOS Project, which involved experiments in three laboratories: wave basin tests at Aalborg University; small-scale wave channel tests at the University

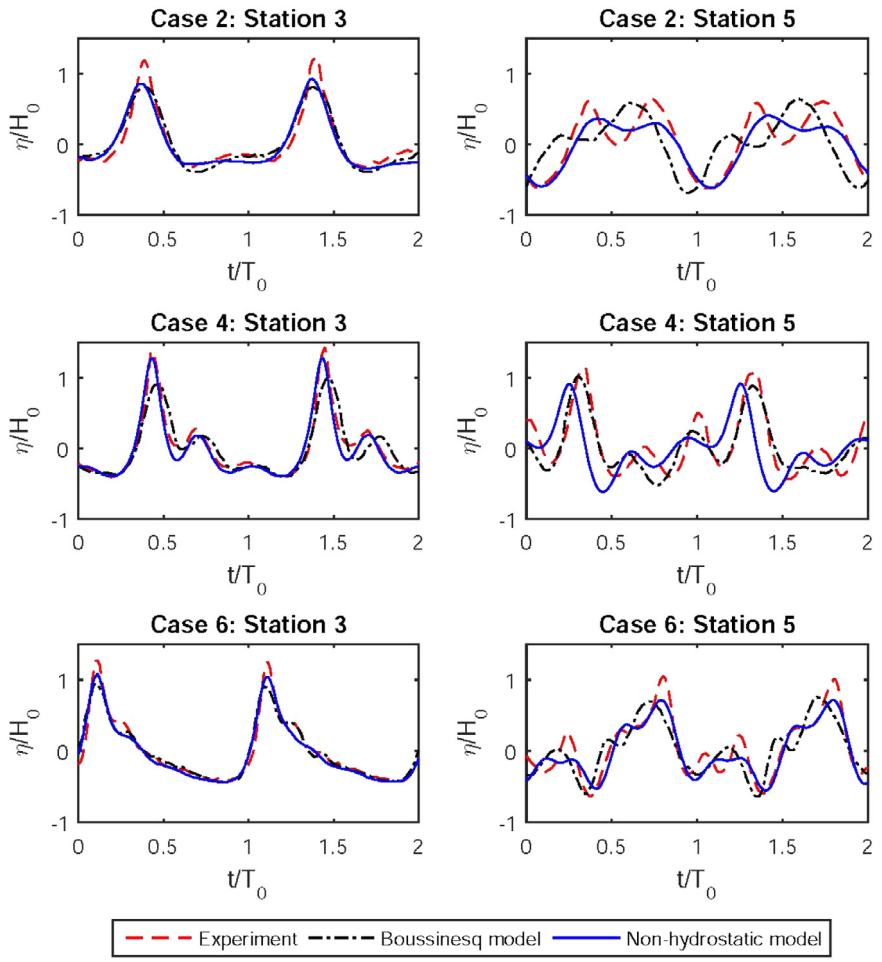

Fig. 8. Comparisons of free surface elevation for cases (2, 4 & 6) of the Ohyama experiment at Stations 3 and 5. H_0 and T_0 are the initial wave height and period, respectively.

Table 7
The computational time of Non-hydrostatic model and Boussinesq model on simulating Case 2 of Ohyama Experiment.

Model	Time (s)
Non-hydrostatic	0.082617
Boussinesq	0.129288

of Cantabria in Santander; and large-scale wave channel tests at the Polytechnic University of Catalonia in Barcelona, all investigating wave interactions with low-crested breakwaters. Detailed descriptions of this project may be found in [12] and the DELOS website (http://www.delos.unibo.it/). Here, we use some of the results of the experiments undertaken at the University of Cantabria that provide information on wave transmission over the breakwater. The wave flume was 24 m long, 0.60 m wide, and 0.80 m high. Waves were generated with a piston-type wavemaker integrated into an active wave absorption system that allowed the absorption of reflected waves from the model. The breakwater was constructed of gravel and was porous. The still water depth away from the breakwater was 0.4 m, and over the crest of the breakwater was 0.05 m. Waves of amplitude 0.05 m were generated and propagated towards the breakwater. Wave breaking occurred on the breakwater crest, causing energy dissipation due to the effects of porosity, inertial, and friction when the wave interacts with the breakwater. In this scenario, all of the effects mentioned are considered to be integrated into the diffusion term alongside the turbulence effect. Therefore, in this subsection, the impact of each property will not be assessed separately. In exchange, we will evaluate the effect of the diffusion term on the energy dissipation, by investigating the diffusion coefficient κ.

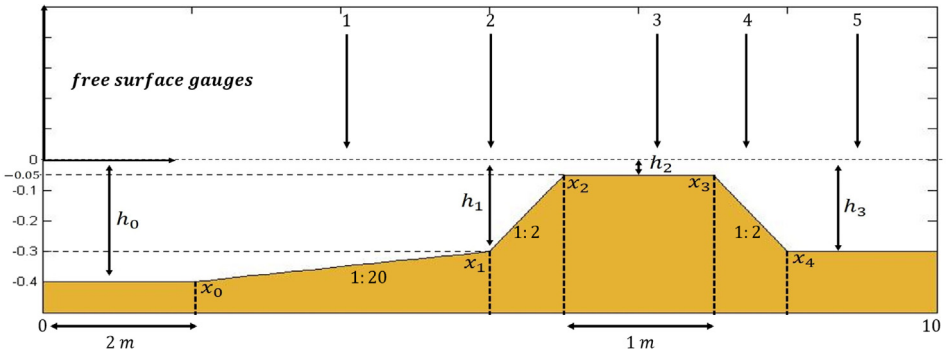

Fig. 9. The illustration of a submerged composite-sloped trapezoidal breakwater used in the simulation and the measurement points of the project.

Table 8
The errors of RANS-VOF and Non-hydrostatic results compared to the experimental data, calculated using Root Mean Square Error (RMSE) method.

Gauge	RMSE (m)	
	RANS-experiment	Nonhydrostatic-experiment
1	0.011575	0.009315
2	0.013790	0.009850
3	0.004935	0.005168
4	0.007950	0.004142
5	0.009136	0.006120

The breakwater cross-section is shown in Fig. 9 and has a composite front slope, as described in [12] and on the DELOS website. Water level gauges corresponding to five locations marked with numbered arrows were used to compare the measurements and numerical model output. Further details of the gauge measurements made in the laboratory experiments may be found in [11]. In the experiments, there was approximately 2 m of uninterrupted flat bottom between the wavemaker and the leading edge of the breakwater slope. A similar set-up was created in the numerical model as shown in Fig. 9, with the wave maker at $x = 0$ and the total domain being 10 m long. Gauges 1, 2, 3, 4, and 5 are positioned at $x = 3.28$ m, 4 m, 5.137 m, 5.602 m and 7.135 m, respectively.

Following this experiment, Zou and Peng [43] have formulated a model based on the Reynolds Averaged Navier–Stokes Solver (RANS) and Volume of Fluid (VOF) surface capturing scheme (RANS-VOF) to approximate the experimental results. Now, we will simulate the wave propagation based on the set-up of the experiment using our non-hydrostatic model and compare the results against the experimental data and RANS-VOF simulation results.

For the simulation, the parameters for the breakwater location are $x_0 = 2$ m, $x_1 = 4$ m, $x_2 = 4.5$ m, $x_3 = 5.5$ m, and $x_4 = 6$ m. The parameters for the depth are $h_0 = 0.4$ m, $h_1 = 0.3$ m, $h_2 = 0.05$ m, and $h_3 = 0.3$ m. The spatial domain of the simulation is [0, 10] which is divided into partitions with a length of $\Delta x = 0.2$ m, while the time step for the numerical computation is $\Delta t = 0.05$ s. Initial conditions are that the fluid is at rest, and there is an absorbing boundary at the right-hand end of the simulation domain. The incoming wave has amplitude of $A = 0.05$ m and period of $T = 1.6$ s, and the Earth's gravitational acceleration is taken as $g = 9.81$ ms^{-2}. All these parameters are used for both models. As the breakwaters are porous and wave breaking occurs on and after the breakwater, diffusion has been included in this set of simulations. Comparisons between our model simulation, RANS-VOF results, and the experimental measurements are shown in Fig. 10. The diffusion coefficient has been treated as a calibration parameter. The results in Fig. 10 are the best fit, achieved with the value of $\kappa = 0.03$ m^{2}s^{-1}.

From Fig. 10, it may be seen that our numerical scheme matches the results from the experimental study very well in terms of amplitude and phase. Overall, the wave amplitudes obtained from our simulation are always lower than those produced by the RANS-VOF simulation and closer to the experimental wave amplitudes. Some distortion might be found in the comparison at all gauges, but we can see that our model approximates the experimental data better than RANS results in terms of the wave skewness, particularly for Gauges 2, 3, and 4.

Table 8 shows the errors obtained from the comparison between RANS-VOF model results and Experimental data, as well as Non-hydrostatic model results and Experimental data. The errors are calculated for all gauges using Root Mean Square Error (RMSE) method. It can be seen that our errors in all gauges are always smaller than RANS-VOF errors, except for the middle one, or Gauge 3. Considering that Gauge 3 is located on top of the breakwater's crest, it means that RANS model can simulate the waves better on top of the crest, while we can approach the experimental data better on other domains. However, the gap between both errors is very small, only about 0.0002, so our model can still be considered a good approximation to the data. Further, Table 9 shows the computational time for both Non-hydrostatic and RANS-VOF

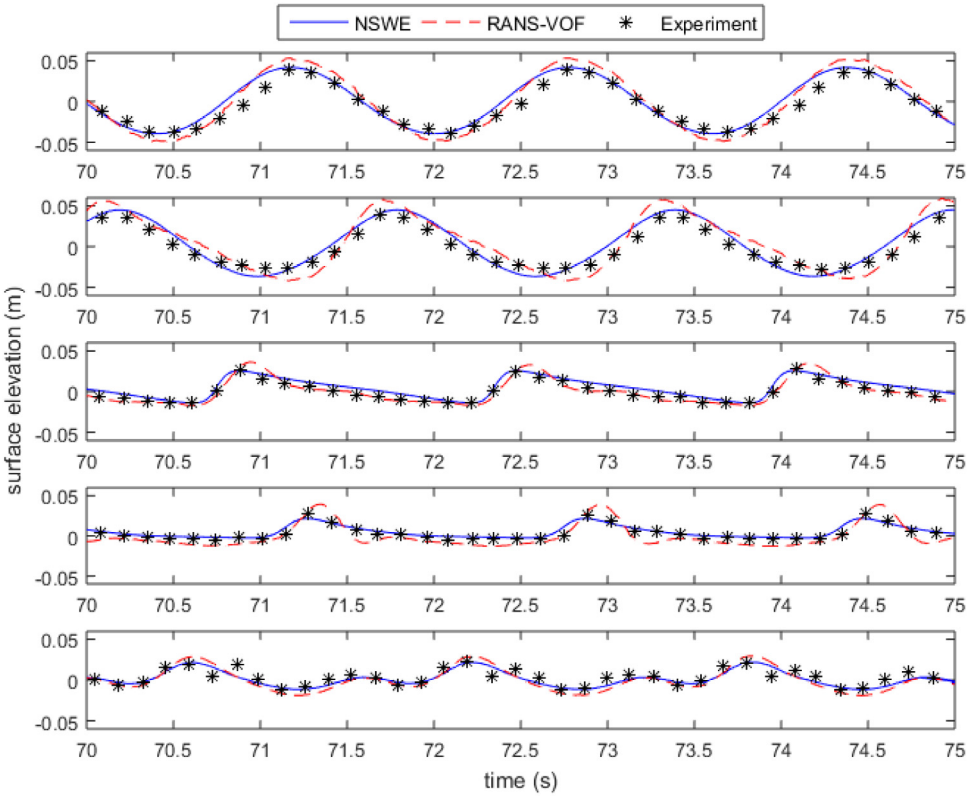

Fig. 10. Comparison of our results against RANS-VOF results and the experimental data from the DELOS Project for Gauges 1, 2, 3, 4, and 5, respectively from top to bottom of the picture.

Table 9
The computational time of Non-hydrostatic model and RANS-VOF model on simulating DELOS project.

Model	Time (s)
Non-hydrostatic	0.093372
Boussinesq	0.148454

models in simulating the DELOS project using computer in which configurations can be found in Table 5. It can be found in Table 9 that the proposed model is faster in simulating the DELOS project compared to RANS-VOF model with same parameters. It can also be seen that the computational time of Non-hydrostatic model is consistent in all three cases that we discuss in this section.

Further, we will investigate the impact of the height and length of the crest, as well as the diffusion coefficient on the wave's evolution. First, we will study how the height of the crest affecting the wave's maximum amplitude and shape. Here, we vary the water depth on top of the crest in the range of 0.05 m $\leq h_2 <$ 0.3 m and set $\kappa = 0$. We simulate the wave propagation and calculate its elevation at the end of the domain ($x = 10$ m) to see its evolution after it passes over the structure. The changes in wave shape and wave amplitude that depend on the value of h_2/h_0 can be seen in Fig. 11.

From Fig. 11, we can clearly see that the smaller the value of h_2/h_0, the smaller the wave transmitted amplitude produced. A smaller value of the ratio means that the water depth on top of the crest is much shallower than the total water depth, which also means that the crest becomes higher. On that note, we can say that the existence of the submerged trapezoidal breakwater structure may significantly attenuate the wave amplitude. Furthermore, we also notice that the shape of the wave becomes smoother as the crest gets closer to the still water level, while when the crest becomes closer, we can see that the wave shape is rougher.

For the second simulation, we will study how the length of the crest ($x_3 - x_2$) affects the wave evolution. In this case, we set the water depth on top of the crest to be $h_2 = 0.05$ m and the crest's length to be in the range of $(0, 4)$ m, while $\kappa = 0$. The simulation is also performed at the end of the domain. Fig. 12 shows how the wave evolves depending on the length of the crest. In Fig. 12, it is shown that as the crest's length increases, the transmitted amplitude decreases. At the same time, the wave shape becomes smoother, which is similar to the previous result. This makes sense, because when

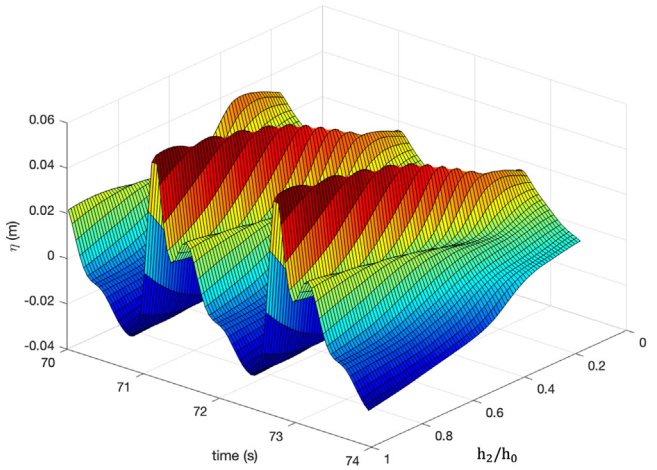

Fig. 11. Changes in wave transmitted amplitude and wave shape depend on the ratio between the water depth on top of the crest and the total water depth.

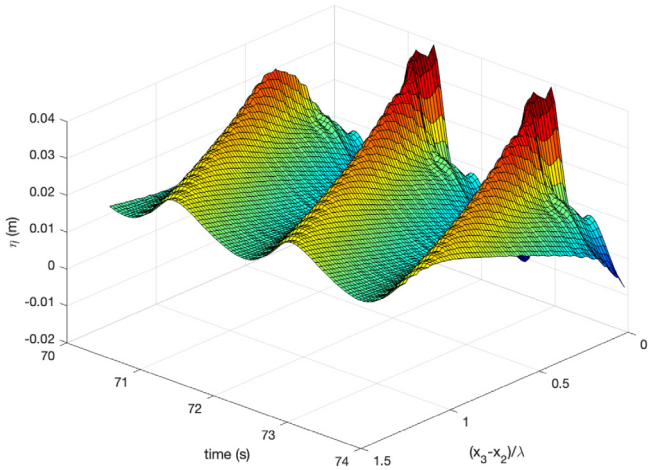

Fig. 12. Changes of wave transmitted amplitude and wave shape depend on the ratio between the length of the crest and wave length ($\lambda = 2\pi/k$), where k is wave number.

the crest's length increases, it means we have more structure to help reduce the wave amplitude and smooth the wave shape.

As stated in the mathematical model section, the existence of the breakwater will bring another effect that will affect the wave evolution, namely turbulence. In this model, turbulence is represented by the diffusion term, which depends on the diffusion coefficient. So, the diffusion coefficient becomes an important part of the model. In this last part of the section, we will discuss how the diffusion effect will affect the wave evolution along with the breakwater structure. Here, we set the parameters to be $h_2 = 0.05$ m with the crest length is $x_3 - x_2 = 1$ m. The diffusion coefficient is varied. The comparison of wave evolution for various values of κ is presented in Fig. 13.

From the simulation results presented in Fig. 13, the diffusion coefficient κ affects the wave evolution similarly to the structure's characteristics. All of them affect the wave shape and wave transmitted amplitude by smoothing the shape and reducing the amplitude. In addition, when the diffusion coefficient is changed from zero to a certain value, the transmitted wave amplitude is reduced significantly by the breakwater. However, when κ changes from 0.5 to a specific value of $\kappa > 0.5$, the submerged breakwater is barely able to lower the wave amplitude. This means, when $\kappa > 0.5$, a certain amount of changes on the coefficient does not affect the transmitted wave amplitude as much as it does when $\kappa < 0.5$.

In addition, we also use the model to simulate the wave evolution over the trapezoidal breakwater for several wave periods within the range of $[1.2, 1.6]$ s. In this scenario, the diffusion coefficient is set to be $k = 0.3$ while other parameters are kept the same, such that we can assess only the effect of changes in wave periods. Fig. 14 shows the wave elevation at Gauge 5 within time period of [70,75] s. It is found that the changes in wave period not only affect the wave phase,

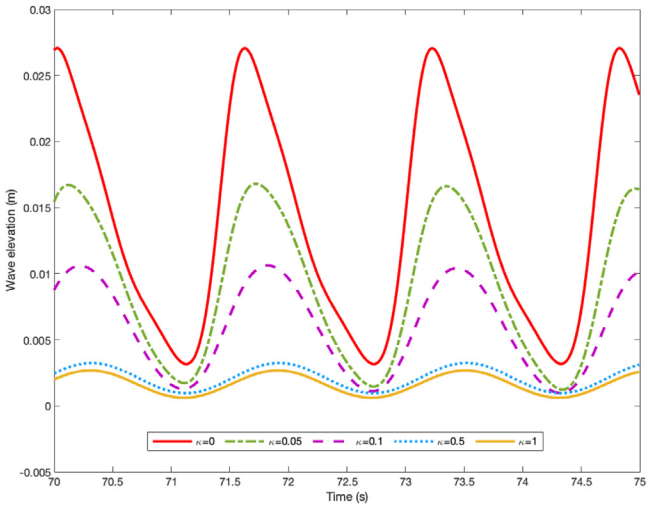

Fig. 13. Wave evolution over composite-slope trapezoidal breakwater structure for various κ.

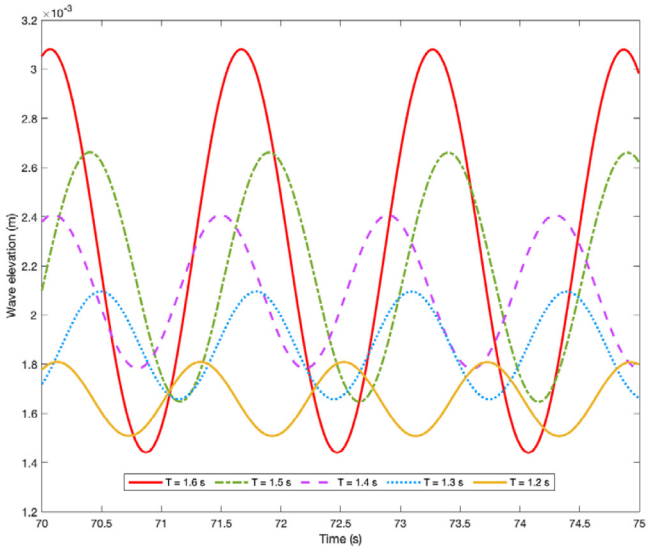

Fig. 14. Wave evolution over composite-slope trapezoidal breakwater for various wave periods with $k = 0.3$ and $A = 0.05$ m.

which is as expected, but also the wave transmitted amplitude. From the simulations, it is found that the wave transmitted amplitude reduce for about 8%–12% every time the wave period shorten by 0.1 s, with average of 10.4525%.

Moreover, several simulations are conducted as well to examine the effect of changes in initial wave amplitude (wave height) on the wave transmitted amplitude. Similarly, in this case, the diffusion coefficient is kept the same ($k = 0.3$) and the wave period is set as $T = 1.6$ s, while now the wave amplitude is varied in the range of $[0.05, 0.1]$ m. The results of these simulations can be found in Fig. 15, which shows that the phase of the waves are the same, since the periods are the same. However, not only the wave transmitted amplitude increases as the initial wave amplitude rises, but the waves are also being lifted all together, which means that even the minimum wave transmitted amplitude is still higher that the still water level ($\eta = 0$). In this case, the wave transmitted amplitudes are significantly increased by 15%–30% each time the initial wave amplitudes are raised by 0.01 m, with average of 21.534%.

5. Conclusion

A one-layer non-hydrostatic model is formulated to investigate the propagation of the wave on a submerged composite-sloped trapezoidal breakwater. This model is solved numerically using a Staggered Finite Volume Method combined with the predictor–corrector procedure. Two test cases were presented to validate the numerical model against

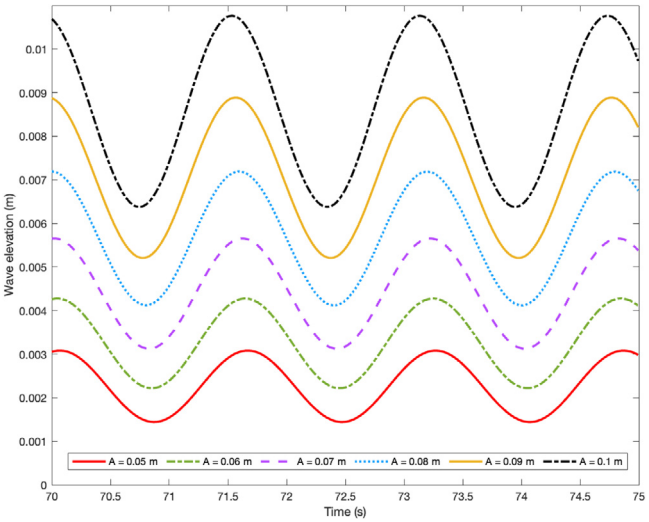

Fig. 15. Wave evolution over composite-slope trapezoidal breakwater for various initial wave amplitudes with $k = 0.3$ and $T = 1.6$ s.

experimental data, and a final case was presented that included both experimental results and output from a RANS computational model. The three cases are experiments involving waves propagating over a submerged breakwater and provide a good test of the model's ability to capture wave transformations, including generation of higher harmonics, shoaling, and dissipation. All test cases showed very good agreement with the experimental data. The final test case demonstrated that in non breaking wave conditions our model results provide a similar level of agreement with experiments as the RANS modelling, but at significantly less computational expense. Further, in cases where gentle wave breaking occurs, turbulent diffusion can be adequately simulated through the inclusion of a simple diffusion term. In future works, this research can be extended to include more than one block of breakwater structure to evaluate the accuracy of the model if wave superposition is involved. Moreover, the type of the n-block breakwaters can also be modified to consider not only rigid and impermeable breakwater, but also porous structure.

Declaration of competing interest

The authors declare that they have no known competing financial interests or personal relationships that could have appeared to influence the work reported in this paper.

Data availability

No data was used for the research described in the article.

Acknowledgment

We acknowledge the financial support from Bandung Institute of Technology and International Mathematical Union.

References

[1] Masselink G, Hughes MG, Knight J. Introduction to coastal processes and geomorphology. 2nd ed.. London, UK: Hodder Education; 2011.
[2] Ahmadian AS. Numerical models for submerged breakwaters: coastal hydrodynamics and morphodynamics. Oxford, United Kingdom: Butterworth-Heinemann; 2016, p. 362.
[3] Lamb H. Hydrodynamics. 6th ed.. New York: Dover; 1932, p. 738.
[4] Jeffreys H. Motion of waves in shallow water. Note on the offshore bar problem and reflection from a bar. Ministry of supply wave report 3, Singapore; 1944.
[5] Mei CC. The applied dynamics of ocean surface waves. Singapore: World Scientific; 1989, p. 768.
[6] Lin P, Liu HW. Analytical study of linear long-wave reflection by a two-dimensional obstacle of general trapezoidal shape. J Eng Mech 2005;131(8):822–30. http://dx.doi.org/10.1061/(ASCE)0733-9399(2005)131:8(822).
[7] Rey V, Belzons M, Guazelli E. Propagation of surface gravity waves over a rectangular submerged bar. J Fluid Mech 1992;235:453–79. http://dx.doi.org/10.1017/S0022112092001186.
[8] Stamos D, Hajj MR. Reflection and transmission of waves over submerged breakwaters. J Eng Mech 2001;127(2):99–105. http://dx.doi.org/10.1061/(ASCE)0733-9399(2001)127:2(99).
[9] Beji S, Battjes JA. Experimental investigation of wave propagation over a bar. Coast Eng 1992;19:151–62. http://dx.doi.org/10.1016/0378-3839(93)90022-Z.

[10] Ohyama T, Kiota W, Tada A. Applicability of numerical models to nonlinear dispersive waves. Coast Eng 1994;24:213–97. http://dx.doi.org/10.1016/0378-3839(94)00033-T.
[11] Garcia N, Lara JL, Losada IJ. 2-D numerical analysis of near-field flow at low-crested permeable breakwaters. Coast Eng 2004;51:991–1020. http://dx.doi.org/10.1016/j.coastaleng.2004.07.017.
[12] Kramer M, Zanuttigh B, Meer JWvander, Vidal C, Gironella FX. Laboratory experiments on low-crested breakwaters. Coast Eng 2005;52(10–11):867–85. http://dx.doi.org/10.1016/j.coastaleng.2005.09.002.
[13] Stagonas D, Warbrick D, Muller G, Magagna D. Surface tension effects on energy dissipation by small scale, experimental breaking wave. Coast Eng 2011;58:826–36. http://dx.doi.org/10.1016/j.coastaleng.2011.05.009.
[14] Suerich-Gulick F, Gaskin SJ, Villeneuve M, Parkinson E. Free surface intake vortices: Scale effects due to viscosity and surface tension. J Hydraul Res 2014;52(4):513–22.
[15] Magdalena I, Atras MF, Sembiring L, Nugroho MA, Labay RSB, Roque MP. Wave transmission by rectangular submerged breakwaters. Computation 2020;8(2):56. http://dx.doi.org/10.3390/computation8020056.
[16] Repousis E, Metallinos A, Memos CD. Wave breaking over submerged breakwaters. In: The 5th international conference on the application of physical modelling to port and coastal protection. 2014, p. 2.
[17] Soukup J, Klimenda F, Skocilas J, Zmindak M. Finite element modelling of shock wave propagation over obstacles. Manuf Technol 2019;19(3):499–507. http://dx.doi.org/10.21062/ujep/319.2019/a/1213-2489/MT/19/3/499.
[18] Magdalena I, Hariz AAA, Farid M, Kusuma MSB. Numerical studies using staggered finite volume for dam break flow with an obstacle through different geometries. Results Appl Math 2021;12:100193. http://dx.doi.org/10.1016/j.rinam.2021.100193.
[19] Wiryanto LH. Wave propagation passing over a submerged porous breakwater. J Eng Math 2011;70:129–36. http://dx.doi.org/10.1007/s10665-010-9419-3.
[20] Williams AN, Wang KH. Flexible porous wave barrier for enchanced wetlands habitat restoration. J Eng Mech 2003;129(1):1–8.
[21] Magdalena I, La'lang R, Mendoza R. Quantification of wave attenuation in mangroves in Manila Bay using nonlinear shallow water equations. Results Appl Math 2021;12:100191. http://dx.doi.org/10.1016/j,rinam.2021.100191.
[22] Firdaus K, Matin AMA, Nurisman N, Magdalena I. Numerical study for Sunda Strait Tsunami wave propagation and its mitigation by mangroves in Lampung, Indonesia. Results Eng 2022;16:100605. http://dx.doi.org/10.1016/j.rineng.2022.100605.
[23] Magdalena I, Michael L. Two layer model for n-emerged porous breakwater on a muddy bottom. Results Appl Math 2022;15:100290. http://dx.doi.org/10.1016/j.rinam.2022.100290.
[24] Tabssum S, Kaligatla RB, Sahoo T. Surface gravity wave interaction with a partial porous breakwater in the presence of bottom undulation. J Eng Mech (ASCE) 2020;146(9):04020088, (1-18).
[25] Sharma M, Kaligatla RB, Sahoo T. Wave interaction with a submerged floating tunnel in the presence of a bottom mounted submerged porous breakwater. Appl Ocean Res 2020;96:102069, (1-12).
[26] Singh S, Kaligatla RB. The combined refraction-diffraction effect on water wave scattering by a vertical flexible-porous structure. J Fluids and Struct 2023;116:103791.
[27] Brocchini M, Dodd N. Nonlinear shallow water equation modeling for coastal engineering. J Waterw Port Coast Ocean Eng 2008;134(2):104–20. http://dx.doi.org/10.1061/(ASCE)0733-950X(2008)134:2(104).
[28] Dingemans MW. Comparison of computations with Boussinesq-like models and laboratory measurements. Report H-1684.12, Delft Hydraulics; 1994, p. 32.
[29] Madsen PA, Murray R, Sörensen OR. A new form of the Boussinesq equations with improved linear dispersion characteristics. Coast Eng 1991;15:371–88. http://dx.doi.org/10.1016/0378-3839(92)90019-Q.
[30] Stoker JJ. Water waves, the mathematical theory with applications. New York: Interscience Publishers Inc.; 1957, p. 609.
[31] Mei CC. Basic gravity wave theory. Handbook of ocean engineering. Texas, United States: Gulf Publishing Co; 1990, p. 1152,
[32] Peregrine DH. Long waves on beaches. J Fluid Mech 1967;27:815–27. http://dx.doi.org/10.1017/S0022112067002605.
[33] Hamm L, Madsen PA, Peregrine DH. Wave transformation in the nearshore zone: A review. Coast Eng 1993;21(1–3):5–39. http://dx.doi.org/10.1016/0378-3839(93)90044-9.
[34] Dingemans MW. Wave propagation over uneven bottoms, part 2. Advanced series on ocean engineering, vol. 13, Singapore: World Scientific; 1997, p. 516.
[35] Lin P, Liu HW. A numerical study of breaking waves in surf zone. J Fluid Mech 1998;359:239–64. http://dx.doi.org/10.1017/S002211209700846X.
[36] Lubin P, Caltagirone JP. In: Ma Q, editor. Large eddy simulation of the hydrodynamics generated by breaking waves. Advances in coastal and ocean engineering, vol. 11, Singapore: World Scientific; 2010, p. 700.
[37] Nwogu OG. Numerical prediction of breaking waves and currents with a Boussinesq model. In: 25th international conference on coastal engineering. 1997, p. 4807–20. http://dx.doi.org/10.1061/9780784402429.374.
[38] Pedlosky J. Geophysical fluid dynamics. 2nd ed.. Berlin, Germany: Springer-Verlag; 1987, p. 710.
[39] Cushman-Roisin B. Introduction to geophysical fluid dynamics. New Jersey: Prentice Hall; 1994, p. 320.
[40] Ames WF. Numerical methods for partial differential equations. London: Thomas Nelson & Sons; 1977, p. 365.
[41] Magdalena I. Non-hydrostatic model for solitary waves passing through a porous structure. J Disaster Res 2016;11(5):1–7. http://dx.doi.org/10.20965/jdr.2016.p0957.
[42] Benjamin TB, Feir JE. The disintegration of wave trains on deep water. Part 1. Theory. J Fluid Mech 1967;27(3):417–30. http://dx.doi.org/10.1017/S002211206700045X.
[43] Zou Q, Peng Z. Evolution of wave shape over a low-crested structure. Coast Eng 2011;58(6):478–88. http://dx.doi.org/10.1016/j.coastaleng.2011.01.001.